Leakage Magnetic Field Suppression Using Dual-Transmitter Topology in EV Wireless Charging

Guodong Zhu[*], Dawei Gao[†], and Shulin Lin[**]

[†,*]State Key Lab of Automotive Safety and Energy, Dept. of Automotive Eng.,
Tsinghua University, Beijing, China
[**]School of Mechanical Eng., University of Science and Technology Beijing, Beijing, China

Abstract

This paper proposes an active leakage magnetic field (LMF) suppression scheme, which uses the dual-transmitter (DT) topology, for EV wireless charging systems (EVWCS). The two transmitter coils are coplanar, concentric and driven by separate inverters. The LMF components generated by the three coils cancel each other out to reduce the total field strength. This paper gives a detailed theoretical analysis on the operating principles of the proposed scheme. Finite element analysis is used to simulate the LMF distribution patterns. Experimental results show that when there is no coil misalignment, 97% of the LMF strength can be suppressed in a 1kW prototype. These results also show that the impact on efficiency is small. The trade-off between LMF suppression and efficiency is revealed, and a control strategy to balance these two objectives is presented.

Key words: Control strategy, Dual-transmitter, EV wireless charging, Finite element analysis, Leakage magnetic field, Wireless power transfer

I. INTRODUCTION

One of the many challenges that wireless power transfer (WPT) faces is leakage magnetic field (LMF) suppression. Excessive exposure to electromagnetic fields is a threat to human health [1]. In addition, LMFs are a potential source of electromagnetic interference to other sensitive equipment. To suppress the LMF in WPT systems, researchers have proposed many effective measures, which can be divided into three main categories: coil design, passive shielding and counter-LMF generation.

The first category focuses on the geometric optimization of coil windings so that less LMF is generated. Coils with reverse windings are studied and three design methods are suggested therein [2]. The authors of [3] proposed a quadruple-coil transmitter (TX), where the current directions of two neighboring coils are opposite for laptop charging applications. The DD and DDQ coils introduced in [4] can reduce the LMF in regions close to the coil center. However, in regions further away they generate a stronger LMF than circular coils. A magnetic field shaping technique that uses a TX coil composed of several windings was introduced in [5] for EV wireless charging systems.

Measures in the second category use soft magnetic materials to guide magnetic flux lines or they use the eddy current in metal plates to offset the incident magnetic field. Soft magnetic materials can improve the mutual inductance and lower the LMF strength on its backside. However, in other regions the LMF strength cannot be effectively suppressed, (see Fig. 4 of [6]). Metallic plates can lower the LMF strength in nearly all regions. However, they can also cause eddy current loss. Usually these two measures are combined to achieve better shielding effectiveness and to reduce loss [6]. Due to their simplicity and effectiveness, techniques of this category are the most widely adopted. Theoretical analyses of magnetic field shielding can be found in [7], [8]. Magnetic structure designs and optimization methods are presented in [9], [10]. In addition, metamaterials can also be used to reduce LMF and to improve coupling at the same time [11].

The third category uses extra coil currents to generate counter-LMF. These currents are generated either through magnetic induction or by reverse winding. An active LMF suppression scheme with feedback control was proposed in [12]. However, it was applied for extremely low frequency magnetic field mitigation and is unsuitable for WPT systems whose operating frequencies are much higher. In [13], a combination of active and passive shielding is adopted for power-frequency magnetic field management. In WPT systems, a popular solution is to use a reactive coil. The authors of [14], [15] demonstrated a resonant reactive LMF shielding scheme with automatic tuning control for online electric vehicles. The authors of [16] proposed a reactive shielding scheme with a phase shifter, which solves contradictions between the current phase angle and the amplitude in the reactive coil. The authors of [17] used a hybrid loop array to improve efficiency and reduce LMF strength. A scheme that connects a TX coil in series with a flux cancelling coil was proposed in [18] to cancel the magnetic field on the backside of the TX. In WPT there are no known articles on active LMF suppression schemes that use an independently-driven coil. In addition, existing solutions cannot achieve an extremely high LMF suppression percentage (e.g., >95%).

This paper proposes a dual-transmitter (DT) LMF suppression scheme based on the counter-LMF generation principle. The underlying circuit theories are analyzed in detail, and a strong LMF suppression ability is demonstrated. Finite element analysis is used to simulate the LMF distribution patterns. In terms of efficiency, the DT-EVWCS (EV wireless charging system) is superior to its single-transmitter (ST) counterparts, which are almost the same as the DT system except that they have only one TX. When the two inverters are properly controlled, MOSFET conduction loss can be reduced and DC to DC efficiency can be improved in DT-EVWCS. Due to the trade-off between LMF suppression and efficiency, a control strategy to balance these two objectives has also been proposed.

The rest of this paper is organized as follows. Section II introduces the operating principles of the proposed scheme. Section III analyzes the LMF distribution patterns generated by three coils and proposes a control strategy to balance the LMF suppression and efficiency. Section IV demonstrates some experimental results. Finally, section V concludes the paper.

II. OPERATING PRINCIPLE OF THE DT-EVWCS

In the DT-EVWCS, two concentric and coplanar TXs are driven by separate inverters, as shown in Fig. 1. Coil 1 is the main TX coil, and coil 2 is the auxiliary TX coil. The LCC compensation topology is used in both TXs because of its constant-current-output feature and increased degrees of freedom in terms of parameter optimization [19]. On the receiver (RX) side, series compensation is adopted because of
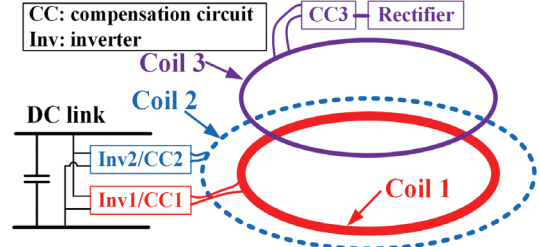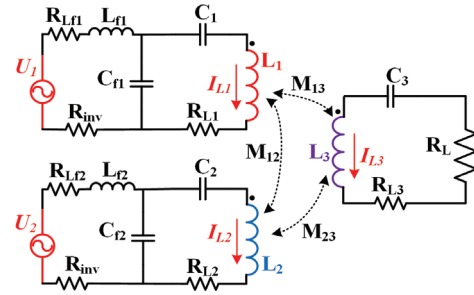

Fig. 1. Simplified structure of the DT-EVWCS.

Fig. 2. Simplified schematic of the DT-EVWCS.

its simplicity. Since compensation circuits are basically bandpass filters, only the fundamental voltage and current components are considered. In this entire paper, the operating frequency is fixed at 85kHz.

The operating principle of the DT-EVWCS can be briefly explained as follows. Two carefully-designed TX coil current phasors generate a magnetic field, where the required voltage is induced in the RX coil. The LMF generated by the three coils cancel each other out to keep the overall LMF strength below a given limit. In addition, the efficiency can be optimized by properly controlling the two TX coil currents.

A. Interactions Among the Three Coils

In Fig. 2, U_1 and U_2 are the inverter output fundamental voltages; R_L is the equivalent load resistance ($R_L = \frac{8}{\pi^2} R_{load}$, where R_{load} is the DC load resistance); L_1 and L_2 are the TX coils; L_3 is the RX coil; M_{12}, M_{23} and M_{13} are the mutual inductances; C_1, C_2, C_3, C_{f1} and C_{f2} are the compensation capacitors; and L_{f1} and L_{f2} are the compensation inductors. The LCC compensation circuit of TX1 comprises L_{f1}, C_{f1}, C_1 and L_1, and TX2 has a similar structure. R_{inv} is the ESR of the MOSFET-based inverter, which is the sum of the MOSFET on-state drain-source resistances on the current conduction path. For the sake of simplicity, the ESRs are omitted in the following analyses except for the efficiency calculation. According to the basic design principle of the LCC compensation topology, $L_{f1}C_{f1} = L_{f2}C_{f2} = \frac{1}{\omega_0^2}$, and the TX coil currents are controlled by the TX input voltages: $I_{L1} = \frac{U_1}{j\omega_0 L_{f1}}$, $I_{L2} = \frac{U_2}{j\omega_0 L_{f2}}$ [19]. On the RX side, $L_3 C_3 = \frac{1}{\omega_0^2}$, where ω_0 is the
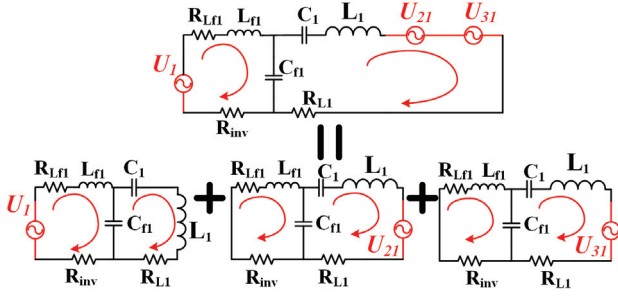
Fig. 3. Superposition of the three components in TX 1.

operating frequency ($2\pi \times 85000$ rad/s). The RX coil current can be obtained as:

$$I_{L3} = \frac{-j\omega_0(M_{13}I_{L1}+M_{23}I_{L2})}{R_L} = \frac{-(M_{13}U_1/L_{f1}+M_{23}U_2/L_{f2})}{R_L}. \quad (1)$$

To obtain a certain $|I_{L3}|$, many combinations of U_1 and U_2 can be used under the condition that $\left|M_{13}\,U_1/L_{f1} + M_{23}\,U_2/L_{f2}\right|$ is equal to a certain value.

TX 1 is driven by three voltages: the inverter output voltage U_1, the induced voltage $U_{21} = -j\omega_0 M_{12}I_{L2}$, and $U_{31} = -j\omega_0 M_{13}I_{L3}$. According to the superposition principle, which is shown in Fig. 3, the output current of inverter 1 can be obtained as:

$$I_{Lf1} = \frac{-j\omega_0 M_{12}I_{L2}}{j\omega_0 L_{f1}} + \frac{-j\omega_0 M_{13}I_{L3}}{j\omega_0 L_{f1}} + \frac{U_1}{j\omega_0 L_{f1}+\left(\frac{1}{j\omega_0 C_{f1}}\|j\omega_0 L_1'\right)}$$

$$= \frac{jM_{12}U_2}{\omega_0 L_{f1}L_{f2}} + \frac{M_{13}(M_{13}U_1/L_{f1}+M_{23}U_2/L_{f2})}{L_{f1}R_L}$$
$$+ \frac{U_1}{j\omega_0 L_{f1}+(-j\omega_0 L_{f1}\|j\omega_0 L_1')}$$

$$= \left[\frac{M_{13}^2}{L_{f1}^2 R_L} + \frac{1}{j\omega_0 L_{f1}+j\omega_0 L_1'/\left(1-\frac{L_1'}{L_{f1}}\right)}\right]U_1$$
$$+ \left(\frac{M_{13}M_{23}}{L_{f1}L_{f2}R_L} + j\frac{M_{12}}{\omega_0 L_{f1}L_{f2}}\right)U_2$$

$$= \left(\frac{M_{13}^2}{L_{f1}^2 R_L} + j\frac{L_1'-L_{f1}}{\omega_0 L_{f1}^2}\right)U_1$$
$$+ \left(\frac{M_{13}M_{23}}{L_{f1}L_{f2}R_L} + j\frac{M_{12}}{\omega_0 L_{f1}L_{f2}}\right)U_2. \quad (2a)$$

Similarly, the output current of inverter 2 is:

$$I_{Lf2} = \left(\frac{M_{23}^2}{L_{f2}^2 R_L} + j\frac{L_2'-L_{f2}}{\omega_0 L_{f2}^2}\right)U_2$$
$$+ \left(\frac{M_{13}M_{23}}{L_{f1}L_{f2}R_L} + j\frac{M_{12}}{\omega_0 L_{f1}L_{f2}}\right)U_1. \quad (2b)$$

Here, $j\omega_0 L_1' = j\omega_0 L_1 + \frac{1}{j\omega_0 C_1}$, $j\omega_0 L_2' = j\omega_0 L_2 + \frac{1}{j\omega_0 C_2}$.

Let $U_1 = |U_1|e^{j0}$ and $U_2 = |U_2|e^{j\theta}$ be the inverter output voltages. Then Equ. (2a) can be changed into:

$$I_{Lf1} = \left(\frac{M_{13}^2}{L_{f1}^2 R_L} + j\frac{L_1'-L_{f1}}{\omega_0 L_{f1}^2}\right)|U_1|(cos0 + jsin0)$$
$$+ \left(\frac{M_{13}M_{23}}{L_{f1}L_{f2}R_L} + j\frac{M_{12}}{\omega_0 L_{f1}L_{f2}}\right)|U_2|(cos\theta + jsin\theta)$$

$$= \left(\frac{M_{13}^2|U_1|}{L_{f1}^2 R_L} + \frac{M_{13}M_{23}|U_2|cos\theta}{L_{f1}L_{f2}R_L} - \frac{M_{12}|U_2|sin\theta}{\omega_0 L_{f1}L_{f2}}\right)$$
$$+ j\left(\frac{L_1'-L_{f1}}{\omega_0 L_{f1}^2}|U_1| + \frac{M_{12}|U_2|cos\theta}{\omega_0 L_{f1}L_{f2}} + \frac{M_{13}M_{23}|U_2|sin\theta}{L_{f1}L_{f2}R_L}\right). \quad (3a)$$

In addition, Equ. (2-b) is equivalent to:

$$I_{Lf2} = e^{j\theta} \cdot \left[\begin{array}{l} \left(\frac{M_{23}^2|U_2|}{L_{f2}^2 R_L} + \frac{M_{13}M_{23}|U_1|cos\theta}{L_{f1}L_{f2}R_L} + \frac{M_{12}|U_1|sin\theta}{\omega_0 L_{f1}L_{f2}}\right) \\ + j\left(\frac{L_2'-L_{f2}}{\omega_0 L_{f2}^2}|U_2| + \frac{M_{12}|U_1|cos\theta}{\omega_0 L_{f1}L_{f2}} - \frac{M_{13}M_{23}|U_1|sin\theta}{L_{f1}L_{f2}R_L}\right) \end{array}\right]. \quad (3b)$$

Ideally, Eqns. (3a and b) should have zero imaginary parts to maximize the TX input power factors. To realize ZVS, the imaginary parts should be slightly negative, which can be realized by adjusting L_{f1}, L_{f2}, C_1 and C_2. A smaller C_1 means a smaller L_1' (L_1' can be negative). Thus, reducing C_1 decreases $imag(I_{Lf1})$, and vice versa. Similarly, C_2 can be used to regulate $imag(I_{Lf2})$. In addition, L_{f1} and L_{f2} can also be adjusted. Apparently, the fully resonant LCC compensation topology [19] ($L_1' = L_{f1}$, $L_2' = L_{f2}$) is not suitable here.

B. Power Flow Path Analysis

Referring to Eqns. (3a and b), it is possible to obtain the input active power to each TX and the total input power:

$$P_{in1} = \frac{1}{2}U_1 \cdot I_{Lf1}$$
$$= \frac{M_{13}^2}{2L_{f1}^2 R_L}|U_1|^2 + \frac{M_{13}M_{23}}{2L_{f1}L_{f2}R_L}|U_1||U_2|\cos(\theta)$$
$$- \frac{M_{12}}{2\omega L_{f1}L_{f2}}|U_1||U_2|\sin(\theta) \quad (4a)$$

$$P_{in2} = \frac{1}{2}U_2 \cdot I_{Lf2}$$
$$= \frac{M_{23}^2}{2L_{f2}^2 R_L}|U_2|^2 + \frac{M_{13}M_{23}}{2L_{f1}L_{f2}R_L}|U_1||U_2|\cos(\theta)$$
$$+ \frac{M_{12}}{2\omega L_{f1}L_{f2}}|U_1||U_2|\sin(\theta) \quad (4b)$$

$$P_{in} = P_{in1} + P_{in2}$$
$$= \frac{M_{13}^2}{2L_{f1}^2 R_L}|U_1|^2 + \frac{M_{23}^2}{2L_{f2}^2 R_L}|U_2|^2$$
$$+ \frac{M_{13}M_{23}}{L_{f1}L_{f2}R_L}|U_1||U_2|\cos(\theta). \quad (4c)$$

In the ST-EVWCS, there is only one power flow path from the TX coil to the RX coil. In Equ. (4c), there are direct power flow paths from the TXs to the RX and a cross-coupling term, which shows that P_{in} is affected by θ.

C. Efficiency Analysis

A passive diode rectifier is adopted in the EVWCS. As a result, power loss on the RX side is determined when the output power and load resistance are fixed. This part focuses on two of the loss terms: the inverter conduction loss and the transmitter loss.

1) Transmitter Efficiency: Transmitter efficiency is defined by $\eta_{trans} = \frac{P_{load}}{P_{loss,TX}+P_{load}}$, where P_{load} is the power consumed on the load resistor, and $P_{loss,TX}$ is the power dissipated on the TX coil ESRs. Strictly speaking, the power losses on the compensation inductors (L_{f1} and L_{f2}) should also be included here. However, they are included in the inverter loss group instead because L_{f1} and L_{f2} are in series with R_{inv}. The power loss on the compensation capacitors is not considered because it is relatively negligible.

Using the law of cosines, the induced voltage in the RX coil is obtained as:

$$|U_3|^2 = (\omega_0 M_{13}|I_{L1}|)^2 + (\omega_0 M_{23}|I_{L2}|)^2$$
$$+2\omega_0^2 M_{13}M_{23}|I_{L1}||I_{L2}|\cos(\theta). \quad (5)$$

Thus:

$$p = \frac{P_{load}}{P_{loss,TX}} = \frac{\frac{|U_3|^2}{2R_L}}{\frac{1}{2}R_{L1}|I_{L1}|^2+\frac{1}{2}R_{L2}|I_{L2}|^2}$$
$$= \frac{\omega_0^2}{R_L} \cdot \frac{M_{13}^2+M_{23}^2 t^2+2M_{13}M_{23}\cos(\theta)t}{R_{L1}+R_{L2}t^2}. \quad (6)$$

Here $t = |I_{L2}|/|I_{L1}|$ is the TX coil current ratio. The derivative of Equ. (6) with respect to t is:

$$\frac{dp}{dt} = \frac{\omega_0^2}{R_L} \cdot$$
$$\frac{-2M_{13}M_{23}\cos(\theta)R_{L2}t^2+2(M_{23}^2R_{L1}-M_{13}^2R_{L2})t+2M_{13}M_{23}\cos(\theta)R_{L1}}{(R_{L1}+R_{L2}t^2)^2}. \quad (7)$$

As can be seen in Fig. 11, $\theta > \frac{\pi}{2}$ is necessary for effective LMF suppression. Therefore, only this case is considered here. The nominator of the second fraction in Equ. (7) is a quadratic function of t, whose leading coefficient is positive. The function value at $t = 0$ is negative. Therefore, the derivative goes from negative to positive as t increases. Since a larger function value of Equ. (6) means a higher η_{trans}, the highest η_{trans} is obtained either at $t = 0$ or $t = +\infty$. In the former case, $\frac{P_{load}}{P_{loss,TX}} = \frac{\omega_0^2 M_{13}^2}{R_L R_{L1}}$; in the latter case, $\frac{P_{load}}{P_{loss,TX}} = \frac{\omega_0^2 M_{23}^2}{R_L R_{L2}}$. These two values correspond to L_1 and L_2 working alone on the TX side. Therefore, the transmitter efficiency of the DT-EVWCS working in the LMF suppression mode should be slightly lower than that of the ST-EVWCS. In this paper, the difference between the ST-EVWCS and the DT-EVWCS is that the former has a single TX (TX1) and this TX uses the fully resonant LCC compensation topology.

2) Inverter Efficiency: Inverter efficiency is defined as $\eta_{inv} = \frac{P_{in}}{P_{loss,inv}+P_{in}}$, where P_{in} is defined in Equ. (4c), and $P_{loss,inv}$ is the conduction loss on R_{inv} and the ESRs of L_{f1} and L_{f2}. Under the soft-switching (ZVS) condition, there is virtually no overlap of the drain-source voltage and drain current at switching instants. Therefore, switching loss is not considered here because ZVS is pursued in this paper. Assuming that the two inverters are identical, $P_{loss,inv}$ is obtained as:

$$P_{loss,inv} = \frac{1}{2}\left(R_{inv} + R_{Lf1}\right)\left(\frac{P_{in1}}{cos\alpha_1|U_1|}\right)^2$$
$$+\frac{1}{2}\left(R_{inv} + R_{Lf2}\right)\left(\frac{P_{in2}}{cos\alpha_2|U_2|}\right)^2. \quad (8)$$

Here $cos\alpha_1$ and $cos\alpha_2$ are the TX input power factors. They should be close to unity to improve inverter efficiency. Obviously, $|U_1|$ and $|U_2|$ can be raised to lower $P_{loss,inv}$, which can be realized by increasing L_{f1} and L_{f2} in the LCC compensation circuits. Nevertheless, the penalty is a lower output power under a limited DC-link voltage (Equ. (4c)).

It is possible for the DT-EVWCS to a achieve higher η_{inv} than the ST-EVWCS when the inverters used in both systems are identical. This can be roughly explained by the following inequality: $P_{in1}^2 + P_{in2}^2 < (P_{in1} + P_{in2})^2$. When $R_{Lf1} = R_{Lf2}$, $cos\alpha_1 = cos\alpha_2 = 1$ and the two inverter output voltages in the DT-EVWCS are equal to those in the ST-EVWCS, the DT-EVWCS has a lower $P_{loss,inv}$. Since the inverter output voltages are actually higher in the DT-EVWCS (see part B of section IV), the difference in $P_{loss,inv}$ between the two systems is larger than that indicated by this inequality.

D. Principles of LMF Suppression

On a specific measurement point in the intended shielding region (ISR, Fig. 6), the magnetic flux density phasor $\boldsymbol{B_{sum}}$ is the sum of three components, each contributed by a separate coil. In addition, the amplitude B_{sum} can be calculated as:

$$B_{sum} = \left|I_{L1}\overrightarrow{K_1} + I_{L2}\overrightarrow{K_2} + I_{L3}\overrightarrow{K_3}\right|$$
$$= \left|I_{L1}\overrightarrow{K_1} + I_{L2}\overrightarrow{K_2} + \frac{-j\omega_0(M_{13}I_{L1}+M_{23}I_{L2})}{R_L}\overrightarrow{K_3}\right|$$
$$= \left|I_{L1}\left(\overrightarrow{K_1} - j\frac{\omega_0 M_{13}}{R_L}\overrightarrow{K_3}\right) + I_{L2}\left(\overrightarrow{K_2} - j\frac{\omega_0 M_{23}}{R_L}\overrightarrow{K_3}\right)\right|. \quad (9)$$

Here $\overrightarrow{K_1}$, $\overrightarrow{K_2}$ and $\overrightarrow{K_3}$ are called magnetic flux density coefficients (MFDCs), which is defined as the magnetic flux density vector generated by 1 ampere of current in a coil when all of the other coil currents are zero. Clearly, the MFDC is a space vector and a function of the measurement position. B_{sum} is a function of three independent variables: $|I_{L1}|$, $|I_{L2}|$ and θ. After the output power constraint in Equ. (1) is imposed, there are two degrees of freedom left.

In the EVWCS prototype, due to the existence of a large metal plate that is used to simulate the car chassis, the magnetic flux lines generated by the three coils are almost coincident when the coil sizes are not too large and the coils are perfectly aligned (Fig. 7(a)). Thus, $\overrightarrow{K_i}$ can be simplified as a scalar and the scalar form is adopted in the rest of this paper. Referring to Equ. (1), it is possible to rewrite Equ. (9) in two forms:
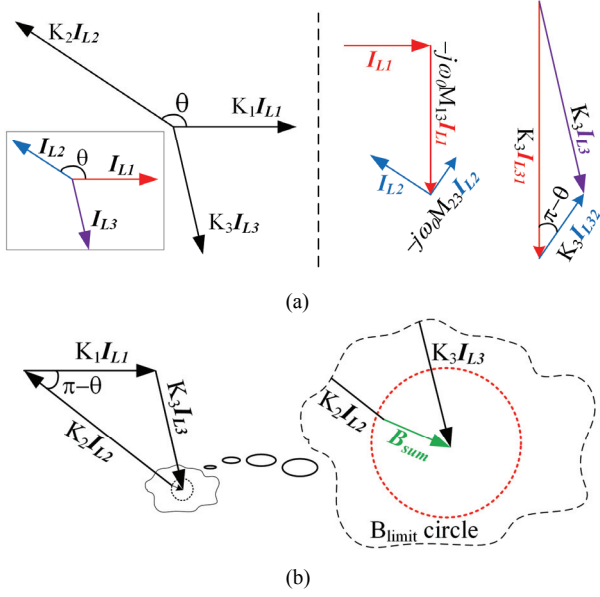
(a)

(b)

Fig. 4. Phasor diagram of the LMF suppression principle. (a) Phasor components. (b) Calculation of $\boldsymbol{B_{sum}}$.
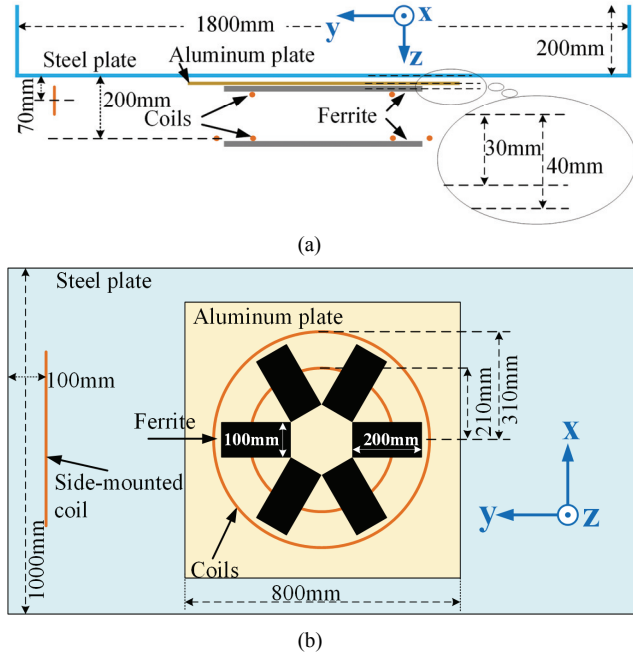

(a)

(b)

Fig. 5. FEA model. (a) Front view. (b) Bottom view.

$$B_{sum} = |I_{L1}K_1 + I_{L2}K_2 + I_{L3}K_3|$$

$$= \left| I_{L1}K_1 + \frac{I_{L3}R_L + j\omega_0 M_{13}I_{L1}}{-j\omega_0 M_{23}}K_2 + I_{L3}K_3 \right|$$

$$= \left| I_{L1}\left(K_1 - \frac{M_{13}}{M_{23}}K_2\right) + I_{L3}\left(K_3 + j\frac{R_L}{\omega_0 M_{23}}K_2\right) \right| \quad (10a)$$

$$B_{sum} = |I_{L1}K_1 + I_{L2}K_2 + I_{L3}K_3|$$

$$= \left| \frac{I_{L3}R_L + j\omega_0 M_{23}I_{L2}}{-j\omega_0 M_{13}}K_1 + I_{L2}K_2 + I_{L3}K_3 \right|$$

$$= \left| I_{L2}\left(K_2 - \frac{M_{23}}{M_{13}}K_1\right) + I_{L3}\left(K_3 + j\frac{R_L}{\omega_0 M_{13}}K_1\right) \right|. \quad (10b)$$
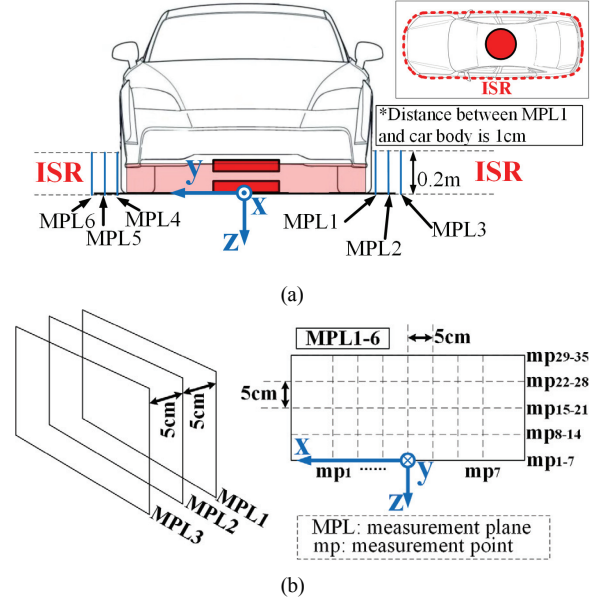

(a)

(b)

Fig. 6. Intended shielding region and measurement point locations. (a) Definition of ISR. (b) Measurement points.

When there is no restriction on the coil currents, any value of B_{sum} is attainable. Specifically, "$B_{sum} = 0$" is called the perfect LMF suppression (PLMFS) working point in this paper. Under this condition, $\boldsymbol{I_{L1}}$ and $\boldsymbol{I_{L2}}$ can be solved as:

$$I_{L1} = \frac{I_{L3}(\omega_0 K_3 M_{23} + jK_2 R_L)}{\omega_0(K_2 M_{13} - K_1 M_{23})} \quad (11a)$$

$$I_{L2} = \frac{I_{L3}(\omega_0 K_3 M_{13} + jK_1 R_L)}{\omega_0(K_1 M_{23} - K_2 M_{13})}. \quad (11b)$$

For a given $B_{limit} > 0$, there are many possible combinations of $\boldsymbol{I_{L1}}$ and $\boldsymbol{I_{L2}}$ that make $B_{sum} < B_{limit}$. To maximize efficiency, a proper control strategy is needed, which will be developed in Section Ⅲ. Fig. 4 shows the LMF suppression principle using phasor diagrams. Multiplying $\boldsymbol{I_{Li}}$ and K_i yields the magnetic flux density phasors in Fig. 4(a). In addition, the two induced voltage components in the RX coil and the two magnetic flux density phasor components are also shown. In Fig. 4(b), $\boldsymbol{B_{sum}}$ is the sum of three phasors. When B_{limit} becomes stricter, the highest achievable η_{trans} becomes lower. The reason for this is simple. If there is no B_{limit} restriction, the maximum η_{trans} is obtained at $\theta = 0$ (Equ. (6)). However, θ should be greater than $\frac{\pi}{2}$ to suppress B_{sum}. Thus, there exists a trade-off between η_{trans} and B_{sum}.

In comparison, the ST-EVWCS has only two coil current phasors. There is only one control variable (the inverter output voltage). Therefore, after the output power constraint is imposed there are no degrees of freedom left. To realize PLMFS, the two coil current phasors need to be opposite in direction and identical in magnitude. Otherwise, they should be null phasors themselves. Both of these conditions are hard to satisfy because the coil current phasors are orthogonal

TABLE I
GEOMETRIC PARAMETERS OF THE EVWCS PROTOTYPE

Parameter	Quantity	Value
W_{steel}	Steel plate width	1800mm
L_{steel}	Steel plate length	1000mm
T_{steel}	Steel plate thickness	1mm
W_{Al}	Aluminum plate width	800mm
L_{Al}	Aluminum plate length	800mm
T_{Al}	Aluminum plate thickness	2mm
N_1	Turn number of coil 1	17
N_2	Turn number of coil 2	8
N_3	Turn number of coil 3	17
r_1	Inner radius of coil 1	180mm
r_2	Inner radius of coil 2	297mm
r_3	Inner radius of coil 3	180mm
R_1	Outer radius of coil 1	245mm
R_2	Outer radius of coil 2	325mm
R_3	Outer radius of coil 3	245mm
μ_r	Relative permeability of ferrite	3300

$(I_{L3} = \frac{-j\omega_0 M_{13} I_{L1}}{R_L})$ when L_3 and C_3 resonate. Hence, there should be an upper limit in the LMF suppression capability for the ST-EVWCS.

III. LMF SUPPRESSION PRINCIPLE

A. LMF Distribution Patterns

Finite element analysis (FEA) is used to simulate the LMF distribution patterns, i.e., the direction and magnitude of the magnetic flux density vectors in the ISR generated by the unit coil currents. The geometric parameters of the EVWCS prototype are listed in Table I. The geometry of the single-layer circular coils, which are made of Litz wire, is shown in Fig. 8(a). A large steel plate on the RX side is used to simulate the car chassis. The TX coil and RX coil are separated by roughly 150mm in the vertical direction, and the ferrite slabs on both sides are arranged as illustrated in Fig. 5.

Some simplifications are made in the FEA model. The thicknesses of the steel plate and aluminum plate, which are 1mm and 2mm, are changed to 10mm and 5mm, respectively. Otherwise, a very fine mesh is required due to the large length-to-thickness ratio of the steel plate (1800:1). L_1, L_2 and L_3 have only one turn in the FEA model, with diameters of 210mm, 310mm and 210mm, respectively. This is also for reducing the model complexity. Due to the employed simplifications, the FEA results are only used to show the overall trend. In Fig. 5, there is also a side-mounted rectangular coil, which is only used for the LMF calculation and is absent in the prototype. The FEA is conducted on COMSOL Multiphysics. The ISR and the measurement points are shown in Fig. 6. The ISR is part of the space outside the car where users are likely to enter under normal circumstances. This should include the regions where the highest LMF strength
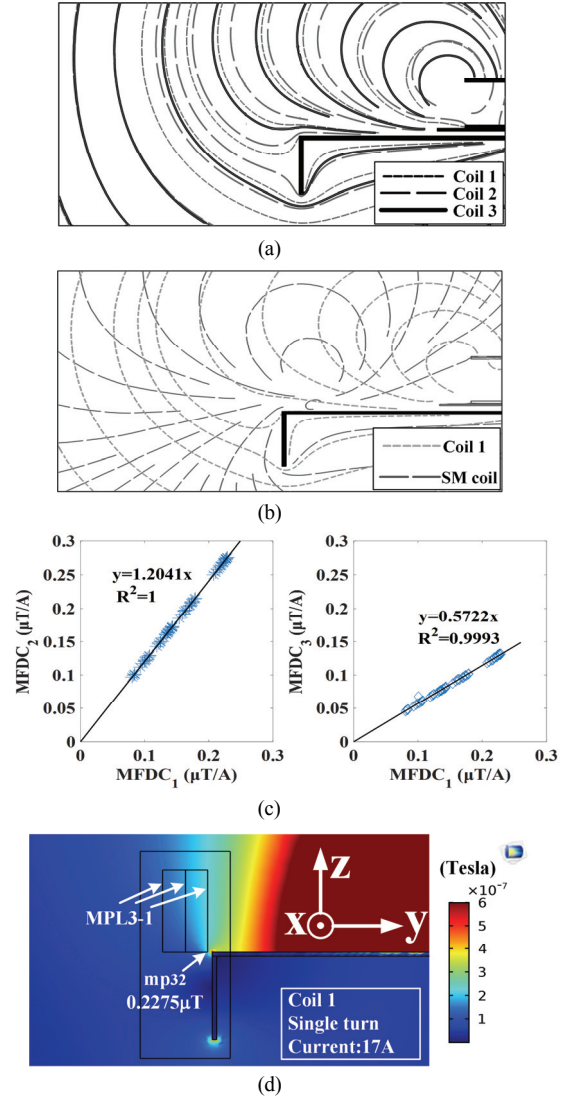

Fig. 7. Simulated LMF distribution patterns. (a) Magnetic flux lines of coils 1-3. (b) Magnetic flux lines of coil 1 and the side-mounted coil. (c) MFDC ratios. (d) Magnetic flux density distribution of coil 1.

appears. It is verified in Fig. 7(d) that the ISR chosen in Fig. 6 can satisfy this requirement.

Simulated LMF distribution patterns are shown in Fig. 7. The MFDC of coil i is obtained when the current in coil i is nonzero and all of the other coil currents are zero. Because coils 1 and 3 have 17 turns in the prototype but only 1 turn in the FEA model, a 17A current is injected into each of them. For coil 2, 7A is injected, where "7" is the originally-chosen turn number of coil 2 (later on "7" is changed to "8" in the prototype). When there is no coil misalignment, the magnetic field vectors generated by the three coils have almost the same directions at all of the points in the ISR. It is worth noting that without the steel plate, the flux lines no longer coincide. When the diameter of coil 2 increases, its flux lines also tend to diverge from those of coil 1. If coil 2 is mounted in other ways, such as the side-mounted type proposed in Fig.
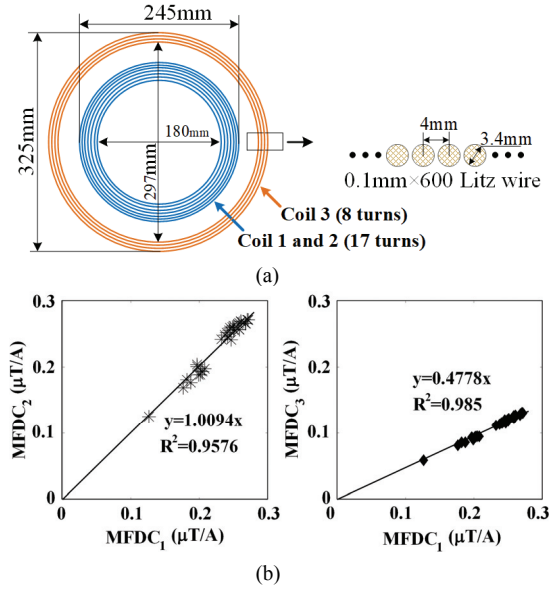
Fig. 8. Coil geometry and measured MFDCs. (a) Coil structure. (b) Measured MFDCs.
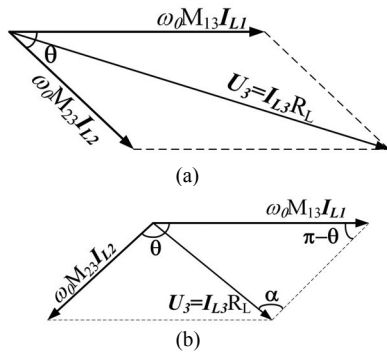

Fig. 9. Summation of induced voltage phasors. (a) $0 < \theta < \frac{\pi}{2}$. (b) $\frac{\pi}{2} < \theta < \pi$.

9 in [14], the LMF distribution pattern of coil 2 is different from that of the other coils. Apparently, the flux lines intersect each other. This shows that perfect LMF suppression is impossible because the sum of two non-parallel space vectors cannot be a null vector unless both of them are null vectors. Theoretically, there should be an upper limit to the LMF suppression capability. The geometric parameters of the single-turn side-mounted coil are shown in Fig. 5. Therefore, the "coincident flux lines" are a precondition for a highly effective LMF suppression. In Fig. 7(c), the MFDC ratios are nearly constant, which is another precondition for high LMF suppression effectiveness. Here $K_2 = 1.2041 K_1$ and $K_3 = 0.5722 K_1$. Constant MFDC ratios, combined with Equ. (10-a), leads to the fact that if K_1 on point A is x times that on point B, then B_{sum} on point A is also x times that on point B (here A and B are two arbitrary points in the ISR). Theoretically, only the B_{sum} on one measurement point is required to evaluate the LMF suppression effectiveness in the whole ISR. If the MFDC ratios are not constant, there exist at

least two points in the ISR whose B_{sum} cannot simultaneously reach a sufficiently low value. Due to symmetry, only the measurement planes 1-3 need to be analyzed. In Fig. 7(c), among all of the measurement points, mp32 has the highest MFDCs (K_1, K_2 and K_3 are 0.2275, 0.2745 and 0.1316 µT/A, respectively). As a result, this point is chosen as a representative. If B_{sum} is below B_{limit} on mp32, then theoretically B_{sum} should be still lower on other points.

In Fig. 8(b), the MFDCs are obtained by measuring the magnetic flux density using a Narda EHP-50 TS when a 1A-amplitude sinusoidal current (85kHz) is injected into the coil under test and the other coils are open-circuited.

According to the linear fitting result, $\frac{K_2}{K_1}$ and $\frac{K_3}{K_1}$ are assumed to be 1.0094 and 0.4778. The strongest LMF strength among all of the measurement points appears on mp32, whose MFDCs are 0.2715, 0.2711 and 0.1309 µT/A, respectively.

B. Control Strategy

When optimizing the three control variables, it is necessary to pay attention to the following two constraints: output power requirement and $B_{sum} < B_{limit}$. The number of control variables is three, so there is still one degree of freedom left. This offers the possibility of efficiency optimization.

The optimum combination of I_{L1} and I_{L2} is hard to solve analytically. However, the following calculation procedure is applicable. Table II gives the electrical parameters, some of which will be used in the calculation. The coil ESRs are

TABLE II
ELECTRICAL PARAMETERS OF THE EVWCS PROTOTYPE

Parameter	Quantity	Value
L_1	Coil 1 inductance	324.5µH
L_2	Coil 2 inductance	93.2µH
L_3	Coil 3 inductance	282.3µH
R_{L1}	ESR of coil 1	0.54Ω
R_{L2}	ESR of coil 2	0.11Ω
R_{L3}	ESR of coil 3	0.55Ω
L_{f1}	Compensation inductor 1	40µH
L_{f2}	Compensation inductor 2	20µH
R_{Lf1}	ESR of L_{f1}	0.10Ω
R_{Lf2}	ESR of L_{f2}	0.07Ω
C_{f1}	Parallel capacitor 1	87.65nF
C_{f2}	Parallel capacitor 2	175.3nF
C_1	Series capacitor 1	11nF
C_2	Series capacitor 2	100nF
C_3	Series capacitor 3	12.42nF
U_{dc}	Maximum DC link voltage	120V
R_{load}	Load resistance	20Ω
R_{inv}	Inverter equivalent resistance	0.12Ω
P_{OUT}	Output power	1kW
M_{12}	Mutual inductance 1-2	42.2µH
M_{23}	Mutual inductance 2-3	21.9µH
M_{13}	Mutual inductance 1-3	75.3µH

measured with an Agilent U1733C at 100kHz (because it does not work at 85kHz).

Step 1. Set the initial value of θ and calculate the highest possible current amplitude $|I_{L1}|_{max}$ under this θ. For $0 < \theta < \frac{\pi}{2}$, $|I_{L1}|_{max} = \frac{|I_{L3}|R_L}{\omega_0 M_{13}}$. For $\frac{\pi}{2} < \theta < \pi$, $|I_{L1}|_{max} = \frac{|I_{L3}|R_L}{\sin(\theta)\omega_0 M_{13}}$. This principle is illustrated in Fig. 9. In the first case, the gap between $|I_{L3}|$ and $|I_{L1}|$ widens as $|I_{L2}|$ increases. Thus, the maximum $|I_{L1}|$ under a given $|I_{L3}|$ is achieved when $|I_{L2}|$ decreases to zero. In the second case, according to the sine theorem, $\frac{\omega_0 M_{13}|I_{L1}|}{\sin(\alpha)} = \frac{|I_{L3}|R_L}{\sin(\pi-\theta)}$ $(\frac{\pi}{2} < \theta < \pi)$. Therefore, $|I_{L1}|$ is maximized at $\alpha = \frac{\pi}{2}$.

Step 2. Decrease $|I_{L1}|$ by an iteration step and calculate $|I_{L2}|$ so that $I_{L3} = \frac{-j\omega_0(M_{13}I_{L1}+M_{23}I_{L2})}{R_L}$ can meet the output power requirement. As mentioned above, B_{sum} is a function of the three control variables $|I_{L1}|$, $|I_{L2}|$ and θ. Since θ is given in *Step 1* and $|I_{L1}|$ is given here, and because of the output power constraint, all three of the degrees of freedom are consumed. Thus, B_{sum} can be uniquely determined.

Step 3. Calculate B_{sum} using Equ. (10a), and check whether $B_{sum} \leq B_{limit}$. If so, calculate η_{trans} with the help of Equ. (6), and calculate η_{inv} with the help of Equ. (8), otherwise discard this combination. Then return to *Step 2.*

Step 4. When $|I_{L1}|$ reaches 0, this increase or decrease θ by an iteration step. Then return to *Step 1.* After all of the reasonable θ values have been tested, pick the combination of θ, $|I_{L1}|$ and $|I_{L2}|$ that results in the highest $\eta_{trans} \cdot \eta_{inv}$.

Based on these four steps, an open-loop and a close-loop control scheme are proposed and shown in Fig. 10. The former is suitable for applications where the MFDCs, mutual inductances and ESRs are known or can be accurately estimated. B_{limit} is a given constant, P_{OUT} is determined by the charging status, and R_L can be calculated from the RX-side information. Based on these quantities, the control strategy in *Step 1 – Step 4* can be used to obtain the optimum $|I_{L1}| - |I_{L2}| - \theta$ combination. Phase shift control and DC-link voltage control are used together to generate the desired $|U_1| - |U_2| - \theta$ parameters. The close-loop control in Fig. 10(b), uses a feedback mechanism. As a result, the "constants" in Fig. 10(a) are not required. There are two constraints: $P_{OUT} = P^*_{OUT}$ and $B_{sum} < B_{limit}$. The efficiency maximization algorithm decreases θ when B_{sum} is low enough and it searches for the optimum $|U_1| - |U_2|$ combination to maximize efficiency while maintaining the required output power. When $B_{sum} > B_{limit}$, θ should be increased. In practice, the $\theta - B_{limit}$ curve in Fig. 11(a), which is the basis of the control algorithm, should be smoothed to make θ a monotonic function of B_{limit}.
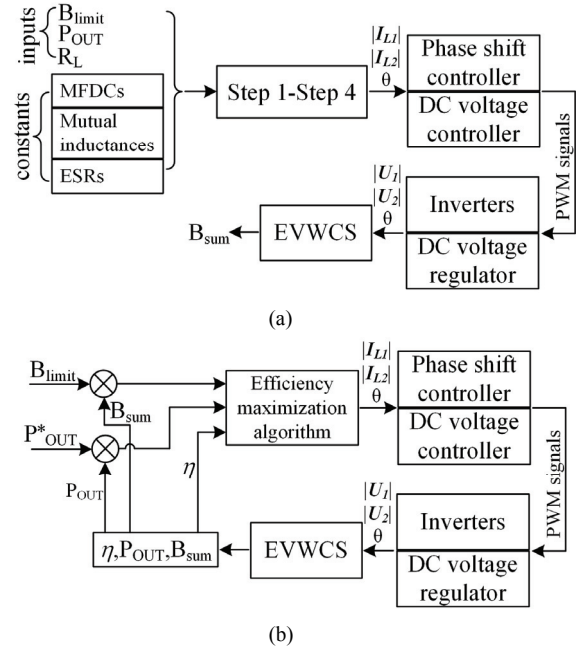

(a)

(b)

Fig. 10. Control block diagrams. (a) Open-loop control. (b) Close-loop control.

Open-loop control is used in this paper. For the DT-EVWCS, the optimum control variables are shown in Fig. 11. When B_{limit} gets less strict, the overall trend is that the optimum θ decreases and the DC to DC efficiency increases. However, after B_{limit} increases beyond 1.23μT, θ no longer decreases. This is due to the four compensation parameters L_{f1}, L_{f2}, C_1 and C_2, whose impact on the TX input power factors were explained in part A of section II, are designed in such a way that the unity power factor of both TXs are reached at $B_{limit} \approx 1.23$μT. If θ is further decreased, a lower η_{inv} is obtained due to the lower TX input power factors. However, η_{trans} might increase. In real applications, another reason for not further decreasing θ is the ZVS condition. The TX input impedance angle becomes negative when θ decreases further, which can also be inferred from Fig. 11(b). The highest theoretical DC to DC efficiency is achieved at the $\theta = 2.225$ point, where both of the TXs have a nearly unity input power factor. Here the receiver efficiency ($\eta_{RX} = \frac{R_L}{R_{L,eq}+R_{L3}}$) is also taken into consideration in the efficiency calculation. However, the rectifier loss is not considered. Fig. 14(b) shows that the LMF on mp32 in the DT-EVWCS can be as low as 0.02μT, which is less than 2% of that in the ST-EVWCS. This means that the LMF can meet strict B_{limit} constraints even at extremely high output power levels. In theory, the LMF strength can reach 0 when the two conditions in Eqns. (11a and b) are satisfied. However, this is not realized here due to discontinuity in the iteration process. In practical applications, the lowest achievable B_{sum} is limited by the voltage regulation accuracy of the inverters. Based on the calculated
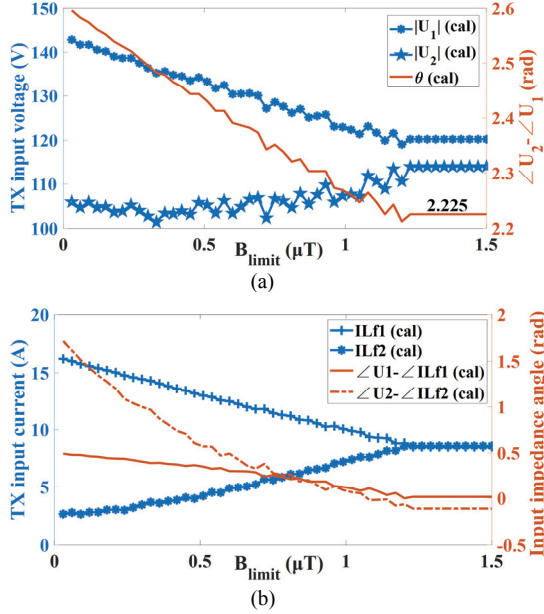
(a)

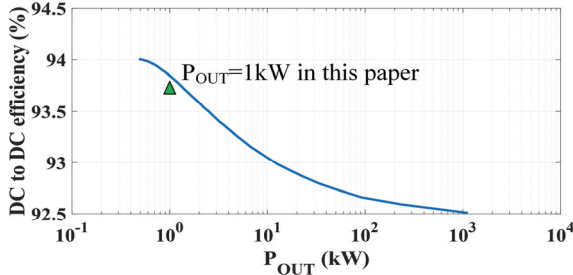Fig. 11. Calculated control variables. (a) TX input voltage. (b) TX input current and impedance angle.

Fig. 12. Theoretical efficiency versus output power at B_{limit} =0.85μT.

efficiency-B_{limit} curve (at $P_{OUT} = 1kW$) in Fig. 14(a), the theoretical efficiency-P_{OUT} curve (at $B_{limit} = 0.85\mu T$) is shown in Fig. 12. It is assumed that P_{OUT} is a quadratic function of the coil current amplitudes, while B_{sum} is a linear function of them. Of course, a real WPT system might exhibit very different behavior under very high-power levels, and the DC link voltage and phase shift angle might deviate from the trajectories in Fig. 11. Thus, Fig. 12 shows only the possible trend. Due to electrical stress and thermal stress considerations, P_{OUT} is fixed at 1kW in the experiments.

IV. MEASUREMENT RESULTS

A. Experimental Setup

The geometric parameters of the EVWCS prototype are shown in Fig. 5 and Table I. The electrical parameters are given in Table II. The ST-EVWCS is identical to the DT-EVWCS, except that it has no TX2 or inverter 2, and it uses the fully resonant LCC compensation topology in TX1 ($C_1 = 12.32nF$). Meanwhile in the DT-EVWCS the compensation

(a)   (b)
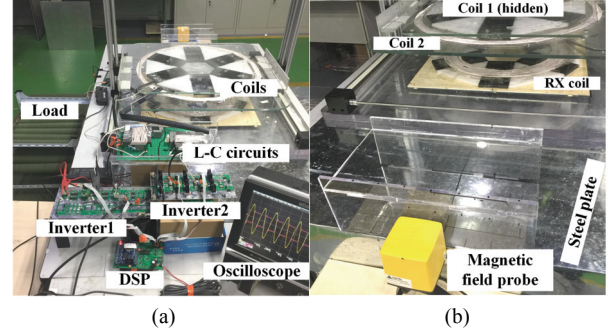
Fig. 13. Experimental setup. (a) Whole system. (b) Measurement position.

capacitor C_1 is redesigned ($C_1 = 11nF$). SiC MOSFETs with $R_{ds,on}$=0.12Ω (Cree C3M0120090J) are used in both of the inverters (2×2 MOSFETs in each leg), which are connected to the same DC source (maximum U_{dc}=120V). The rectifier diodes on the RX side are IXYS DPG15I400PM. Phase shift control is used to regulate the inverter output voltage and the output power is fixed at 1kW. Meanwhile, the DC link voltage is manually regulated. A Teledyne LeCroy Waverunner 610Zi is used for signal measurement. The LMF strength is measured using a NARDA EHP-50 TS. The two inverters in the DT-EVWCS are controlled by the same DSP (TMS320F28335) controller. As a result, driving signal synchronization is easily achieved. The experimental setup is shown in Fig. 13.

B. Measurement Results

In the ST-EVWCS, the DC link voltage is increased gradually until the output power reaches 1kW while the inverter conduction angle is fixed at 180 degrees. Inverter soft switching is realized in the experiment. In the DT-EVWCS, the optimum combinations of U_1 and U_2 in Fig. 11(a) are used as a reference. Due to unavoidable errors, the actual inverter output voltages are tuned around their theoretical optimum values. The DC link voltage control and the phase shift control are used together. Thus, only one of the inverters requires a phase shift. The 120V limit was not exceeded in all of the tests. The results are shown in Figs. 14(a and b). The measured DC to DC efficiency is lower than the theoretical values. However, the trend is the same. The lowest B_{sum} achieved is 0.06μT, and the DC to DC efficiency at this working point is 92.1%. When compared to 1.97μT in the ST-EVWCS, the LMF strength can be reduced by 97%. The highest DC to DC efficiency is 93.6%, which is 2% higher when compared to that of the ST-EVWCS. The trade-off between the LMF strength and efficiency is experimentally validated, and the effectiveness of the open-loop control strategy is also shown, i.e., a higher efficiency is achievable when B_{limit} increases. Although η_{trans} and η_{inv} are not measured separately due to practical difficulties, it can be seen from the theoretical analysis that η_{trans} is lower in the DT-EVWCS, whereas η_{inv} is higher, as explained in
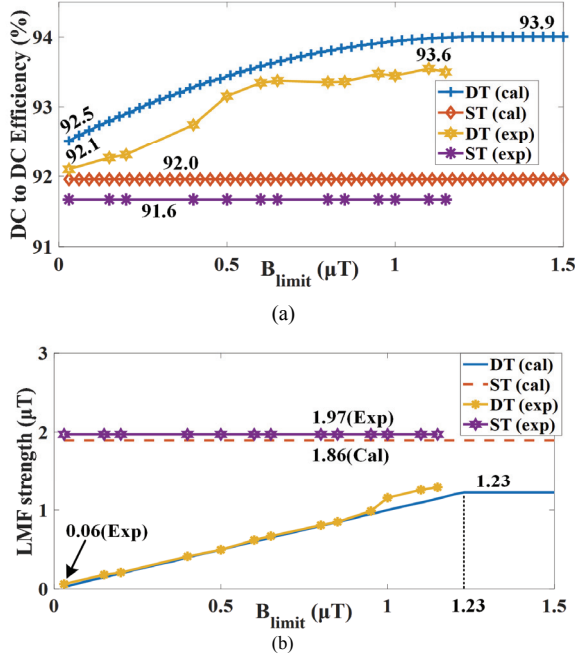
Fig. 15. Simulated LMF distribution at the PLMFS point.

Fig. 14. Calculated and measured efficiency and LMF strength on mp32 in the DT-EVWCS and ST-EVWCS. (a) DC-to-DC efficiency. (b) LMF strength.

part C of section II. In the LTspice simulation, it was observed that at the $B_{sum} = 0.06\mu T$ working point, $\eta_{inv} = 97.30\%$ and $\eta_{trans} \cdot \eta_{RX} = 94.96\%$. In addition, in the ST-EVWCS the two numbers are 95.36% and 96.34%, respectively. At the $B_{sum} > 1.23\mu T$ working points, the three control variables are constant. The two numbers are 98.53% and 95.26% respectively. The price paid for a high LMF suppression capability is an extra TX and lower η_{trans} when compared to the ST-EVWCS. In addition, the price paid for a higher η_{inv} is twice the inverter cost and a higher demand on the DC link voltage (when compared to the data in Fig. 11(a), the fundamental inverter output voltage in the ST-EVWCS is 95.6V in amplitude). ZVS is realized in most of the tests due to the variable DC link voltage control, which reduces the required phase shift angle. In some tests one of the four half-bridges is hard-switched. However, the effect on efficiency is small and the overall efficiency performance is satisfactory.

C. Discussion

Since the ISR is in 3-D space, which increases the difficulty in accurately measuring and clearly presenting the LMF strength on all of the measurement points, the LMF data on only one point (mp32) are experimentally measured. To complement the experimental results, the simulated LMF distribution at the PLMFS working point is presented in Fig. 15. The coil currents used in the simulation are calculated based on simulated MFDCs. The LMF on mp32 is 0.016μT, while the highest strength in the ISR is 0.042μT. The highest LMF strength does not appear on mp32. This is due to the fact

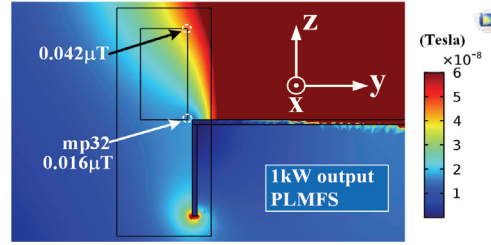that the flux lines generated by the three coils are not strictly coincident and the MFDC ratios are not perfectly constant. At the PLMFS point, a slight error in the MFDC can result in a huge difference in B_{sum}.

At the same time, a manual evaluation process was conducted by moving the field probe in the ISR. It was observed that the magnetic flux density on most of the points in the ISR is lower than that on mp32. This is especially true on points further away from the coil center in the y-coordinate direction. There are some points located near mp32 whose B_{sum} is slightly higher than mp32. This is due to the fact that the point with the highest MFDC appears on a point other than mp32, as is shown in Fig. 7(d). The point mp32 has the highest MFDCs among all of the measurement points instead of among all the points. Overall, the experimental results coincide well with the theoretical analysis.

However, there are still some drawbacks. (1) Only the perfect alignment case is considered here. However, in practical applications, LMF suppression effectiveness is seriously impaired by coil misalignment, as has been observed in the experiment. Due to page limits, this topic is not discussed in this paper. (2) A steel plate is used to simulate the car chassis. However, a real car chassis is a lot more complex in terms of geometry. How this would affect the LMF distribution patterns deserves more in-depth research. (3) The inverter efficiency analysis should be improved to include both harmonic current loss and switching loss.

Despite these drawbacks, the most important finding is that LMF strength can be effectively suppressed by adding an extra TX coil driven by a separate inverter, and that the trade-off between efficiency and LMF suppression can be balanced by a simple control strategy. The DT-EVWCS is superior to the ST-EVWCS in that it can theoretically realize perfect LMF suppression without seriously lowering efficiency due to more control degrees of freedom.

V. CONCLUSION

This paper proposes a novel LMF suppression scheme using the dual-transmitter topology, which is aimed at high-power EV wireless charging applications. The operating principles of the DT-EVWCS are explained. The LMF distribution patterns are simulated via finite element analysis. When there is a large steel plate and the coils are perfectly

aligned, the magnetic flux lines generated by different coils are almost coincident and the MFDC ratios are stable, which are the two preconditions for high LMF suppression capability. A 97% reduction in leakage magnetic flux density is experimentally achieved. Meanwhile, a simple control strategy is proposed to balance the LMF suppression and efficiency.

Due to practical restrictions, only open-loop control was implemented in this paper, and the magnetic couplers (including the coils, ferrite slabs and metal plates) were constructed based on experience. Further research is required in terms of close-loop feedback control, performance under coil misalignment, variable-load/variable-power conditions, circuit parameter optimization and magnetic coupler optimization.

ACKNOWLEDGMENT

REFERENCES

[1] E. Litvak, K. R. Foster, and M. H. Repacholi, "Health and safety implications of exposure to electromagnetic fields in the frequency range 300 Hz to 10 MHz," *Bioelectromagnetics*, Vol. 23, No. 1, pp. 68-82, 2002.

[2] S. Y. Choi, B. W. Gu, S. W. Lee, W. Y. Lee, J. Huh, and C. T. Rim, "Generalized active EMF cancel methods for wireless electric vehicles," *IEEE Trans. Power Electron.*, Vol. 29, No. 11, pp. 5770-5783, Nov. 2014.

[3] S. Y. Ahn, H. H. Park, and J. H. Kim, "Reduction of electromagnetic field (EMF) of wireless power transfer system using quadruple coil for laptop applications," in *Proc. IEEE Microwave Workshop Ser. Innov. Wireless Power Transm.*, pp. 65-68, 2012.

[4] M. Budhia, J. T. Boys, G. A. Covic, and C. Y. Huang, "Development of a single-sided flux magnetic coupler for electric vehicle IPT charging systems," *IEEE Trans. Ind. Electron.*, Vol. 60, No. 1, pp. 318-328, Jan. 2013.

[5] C. W. Chiang, "Wireless charging system with magnetic field shaping for electric vehicles," in *Proc. World Electric Vehicle Symp. Exhibition*, pp. 1-5, 2013.

[6] H. Kim, J. Cho, S. Ahn, J. Kim, and J. Kim, "Suppression of leakage magnetic field from a wireless power transfer system using ferrimagnetic material and metallic shielding," in *Proc. IEEE Int. Symp. Electromagn. Compat.*, pp. 640-645, 2012.

[7] Y. Du, T. C. Cheng, and A. S. Farag, "Principles of power-frequency magnetic field shielding with flat sheets in a source of long conductors," *IEEE Trans. Electromagn. Compat.*, Vol. 38, No. 3, pp. 450-459, Aug. 1996.

[8] P. R. Bannister, "New theoretical expressions for predicting shielding effectiveness for the plane shield case," *IEEE Trans. Electromagn. Compat.*, Vol. EMC-10, No. 1, pp. 2-7, Mar. 1968.

[9] A. Dolara, S. Leva, M. Longo, F. Castelli-Dezza, and M. Mauri, "Coil design and magnetic shielding of a resonant wireless power transfer system for electric vehicle battery charging," in *Proc. IEEE Int. Conf. Renewable Energy Res. Appl.*, pp. 200-205, 2017.

[10] M. Budhia, G. A. Covic, and J. T. Boys, "Design and optimization of circular magnetic structures for lumped inductive power transfer systems," *IEEE Trans. Power Electron.*, Vol. 26, No. 11, pp. 3096-3108, Nov. 2011.

[11] Y. Cho, S. Lee, D. H. Kim, H. Kim, C. Song, S. Kong, J. Park, C. Seo, and J. Kim, "Thin hybrid metamaterial slab with negative and zero permeability for high efficiency and low electromagnetic field in wireless power transfer systems," *IEEE Trans. Electromagn. Compat.*, Vol. 60, No. 4, pp. 1001-1009, Aug. 2018.

[12] C. Buccella, M. Feliziani, and V. Fuina, "ELF magnetic field mitigation by active shielding," in *Proc. IEEE Int. Symp. Ind. Electron.*, pp. 994-998, 2002.

[13] M. L. Hiles, R. G. Olsen, K. C. Holte, D. R. Jensen, and K. L. Griffing, "Power frequency magnetic field management using a combination of active and passive shielding technology," *IEEE Trans. Power Del.*, Vol. 13, No. 1, pp. 171-179, Jan. 1998.

[14] S. Kim, H. H. Park, J. Kim, J. Kim, and S. Ahn, "Design and analysis of a resonant reactive shield for a wireless power electric vehicle," *IEEE Trans. Microw. Theory Techn.*, Vol. 62, No. 4, pp. 1057-1066, Apr. 2014.

[15] J. Shin, S. Shin, Y. Kim, S. Ahn, S. Lee, G. Jung, S.-J. Jeon, and D.-H. Cho, "Design and implementation of shaped magnetic-resonance-based wireless power transfer system for roadway-powered moving electric vehicles," *IEEE Trans. Ind. Electron.*, Vol. 61, No. 3, pp. 1179-1192, Mar. 2014.

[16] H. Moon, S. Kim, H. H. Park, and S. Ahn, "Design of a resonant reactive shield with double coils and a phase shifter for wireless charging of electric vehicles," *IEEE Trans Magn.*, Vol. 51, No. 3, pp. 1-4, Mar. 2015.

[17] S. Lee, Y. Cho, H. Kim, C. Song, S. Jeong, and J. Kim, "Design and analysis of hybrid loop-array for high efficiency and low EMF level in wireless high power transfer system," in *Proc. IEEE Wireless Power Transfer Conf.*, pp. 1-3, 2017.

[18] A. Tejeda, C. Carretero, J. T. Boys, and G. A. Covic, "Ferrite-less circular pad with controlled flux cancelation for EV wireless charging," *IEEE Trans. Power Electron.*, Vol. 32, No. 11, pp. 8349-8359, Nov. 2017.

[19] S. Li, W. Li, J. Deng, T. D. Nguyen, and C. C. Mi, "A double-sided LCC compensation network and its tuning method for wireless power transfer," *IEEE Trans. Veh. Technol.*, Vol. 64, No. 6, pp. 2261-2273, Jun. 2015.

Guodong Zhu was born in Zhejiang, China, in 1995. He received his B.S. degree in Automotive Engineering from Tsinghua University, Beijing, China, in 2017, where he is presently working towards his Ph.D. degree in Power Engineering and Engineering Thermo-Physics. His current research interests include wireless power transfer and its optimization.

Dawei Gao was born in Jilin, China, in 1971. He received his B.S. degree from Southwest Jiaotong University, Sichuan, China, in 1992; and his Ph.D. degree from the North China Electric Power University, Beijing, China, in 2001. From 2001 to 2003, he was a Postdoctoral Researcher; from 2003 to 2005, he was an Assistant Researcher; and since 2005, he has been an Associate Researcher in the Department of Automotive Engineering, Tsinghua University. He is the author of more than 50 papers published in journals and conference proceedings, and has produced more than 35 inventions. His current research interests include DC-DC converters, electric vehicle wireless power transfer, automotive power electronics, electric drives, and electric vehicle powertrain optimization.

Shulin Lin was born in Fujian, China, in 1994. He received his B.S. degree in Mechanical Engineering from the University of Science and Technology Beijing, Beijing, China, in 2017, where he is presently working towards his M.S. degree in Electrical Engineering. His current research interests include electric vehicle wireless charging systems in both static and dynamic applications.